



# Piezoresistive behavior of DLP 3D printed CNT/polymer nanocomposites under monotonic and cyclic loading

Omar Waqas Saadi<sup>1</sup> · Andreas Schiffer<sup>1</sup> · S. Kumar<sup>2</sup>

Received: 20 October 2022 / Accepted: 15 February 2023 / Published online: 17 March 2023  
© The Author(s) 2023

## Abstract

This study examines the piezoresistive behavior of MWCNT/polymer composites fabricated by the digital light processing (DLP) technique. A photocurable nanocomposite resin feedstock possessing low viscosity with excellent printability and high conductivity was developed for DLP 3D printing of bulk and cellular geometries. By optimizing the resin composition and synthesis route, electrical percolation was achieved at an ultra-low MWCNT loading of 0.01 phr (parts per hundred resin), providing a conductivity of  $3.5 \times 10^{-5} \text{ S m}^{-1}$ , which is significantly higher than the values reported in the extant works for similar nanocomposites. Reducing the MWCNT content also enhanced the piezoresistivity of the nanocomposite due to longer inter-MWCNT distances in the percolating conductive network. Under quasi-static tensile loading, the nanocomposite with 0.01 phr MWCNT loading showed gauge factors of 2.40 and 4.78, corresponding to the elastic and inelastic regime, respectively. Quasi-static cyclic tensile tests with constant strain amplitudes (within elastic regime) revealed that the response of the nanocomposite was affected by viscoelastic deformation, which caused significant changes in the material's strain sensing performance between consecutive load cycles. Finally, the developed resin was used to realize a self-sensing gyroid lattice structure, and its strain and damage sensing capabilities were demonstrated.

**Keywords** Strain sensing · Additive manufacturing · Multifunctional composite · Digital light processing · Photocurable resin · Self-sensing

## 1 Introduction

The scientific interest in additive manufacturing (AM) technology has grown exponentially in the previous decade [1–4]. AM technology, also known as 3D printing, enables the fabrication of 3D objects with complex geometries in a single step based on computer-aided design (CAD) models [2]. Since 3D printing is a relatively simple and cost-effective method to create materials with complex architecture and tunable

mechanical/functional attributes, it has been used for a wide range of emerging applications, including scaffolds for tissue engineering [5, 6], structural electronics [7], wearable devices [8], and chemical sensing [9].

Nowadays, a wide range of materials can be 3D printed: polymers, metals, ceramics, and their composites. In particular, polymers and polymer matrix composites are extensively processed via 3D printing due to their low manufacturing cost, and ease of processing. Polymer AM processes can be broadly divided into three main categories: (i) processes that involve curing of liquid resins or inks, such as digital light processing (DLP), direct ink writing (DIW), and stereolithography (SLA), (ii) processes based on sintering/melting of polymer powder such as selective laser sintering (SLS), and selective laser melting (SLM) [10], and (iii) processes based on melting/fusing of thermoplastic filament feedstock, also known as fused deposition modeling (FDM) [4]. Since liquid resins can be easily mixed with a variety of micro and/or nano-fillers, DLP and SLA are highly suitable for the manufacture of functional materials [11]. The extensive literature in the field of photopolymers facilitates

✉ Andreas Schiffer  
andreas.schiffer@ku.ac.ae

✉ S. Kumar  
s.kumar@eng.oxon.org

Omar Waqas Saadi  
100049378@ku.ac.ae

<sup>1</sup> Department of Mechanical Engineering, Khalifa University of Science and Technology, Main Campus, P.O. Box 127788, Abu Dhabi, United Arab Emirates

<sup>2</sup> James Watt School of Engineering, University of Glasgow, Glasgow G12 8LT, UK

the selection of optimal resin formulations for enhanced functional/mechanical properties while also satisfying the requirements of the 3D printing process [12]. Indeed, the development of 3D printable photopolymeric composite resins is a key area in research because they can be used to fabricate complex structures for an array of functional devices at a relatively low cost.

Conductive materials are a particularly important subcategory of 3D printed functional materials since they can be utilized as electrodes or conducting elements for signal transmission, heating, sensing [4], and energy storage applications [13]. Among various conducting nanofillers, CNTs have been most widely used in the fabrication of electrically conductive nanocomposites with conventional manufacturing methods [14] as well as 3D printing techniques [15–20]. The CNTs, if sufficiently incorporated, can create a percolating network of conductive paths in the polymer matrix, increasing the overall conductivity of the nanocomposite by several orders of magnitude. Acrylic [20] and UV-cured epoxy [21] CNT composites have been studied previously. However, due to their strong van der Waals interactions and high aspect ratio, CNTs become entangled and bundled, resulting in agglomeration and segregation of these nanofillers in the composites [22].

While FDM 3D printing of electrically conductive polymers has received considerable attention in the recent past [4, 15, 23–29], the development of electrically conductive photoresin-based nanocomposites and the study of their electrical and piezoresistive behavior has received less attention. Much of the existing literature on this subject relied on the SLA method [16, 30–37]. Valencia et al. [31] investigated the fabrication of 3D printed composite structures with remarkable electrical properties achieved via in-situ fabrication of silver nanoparticles (AgNPs). Chiappone et al. [38] used the DLP technique to print 3D hybrid structures by in situ production of inorganic nanoparticles. Electrical properties of complex 3D structures printed with PEGDA and in situ prepared AgNPs were also studied [39]. While in situ generation of conductive nanofillers has shown success in creating hybrid multifunctional structures, it is more common to add conductive (solid) fillers to the liquid resins prior to the 3D printing process [40]. For example, Gonzalez et al. [19] prepared an acrylic based UV curable resin incorporated with MWCNTs to study the electrical behavior of DLP-enabled nanocomposite samples. Further, Mu et al. [20] used the DLP technique to print CNT-based conductive composites and studied their piezoresistive response under monotonic and cyclic tensile loads. A recent study on DLP-enabled CNT-based nanocomposites reported a reduced electrical percolation threshold as well as good strain sensitivity with a gauge factor ranging from 2 to 3 [41]. While the studies cited above [19, 20, 41] succeeded in fabricating electrically

conductive and piezoresistive nanocomposites via DLP 3D printing, there is still an enormous potential for further optimization of resin formulations, process parameters, and post-treatment routes to realize complex 3D structures with integrated strain- and/or damage sensing capabilities.

The aim of this study is to investigate the piezoresistive and mechanical behavior of DLP 3D printed MWCNT/acrylic nanocomposites. Optimal MWCNT concentrations and printing parameters are discovered by analyzing electrical conductivity, viscosity, and scanning electron microscope (SEM) images. Monotonic and cyclic tensile tests are performed on bulk samples to examine the mechanical properties of the 3D printed MWCNT nanocomposites, while in situ measurements of the sample's electrical resistance give insight into their piezoresistive characteristics. Finally, the developed nanocomposite resin is put to use by fabricating a 3D cellular (gyroid) structure to investigate its potential use as a self-sensing device.

## 2 Materials and methods

### 2.1 Materials

The resin used in this study is a mixture of commercially available photoresin (PlasClear) and tripropylene glycol diacrylate (TPGDA). TPGDA was added to decrease the viscosity of the resin mixture. The photoinitiator used was diphenyl (2,4,6-trimethyl benzoyl) phosphine oxide, commonly known as TPO. PlasClear was purchased from Asiga (Alexandria, Australia). The rest of the chemicals were purchased from AllPlace, Shandong, China. The fillers used were MWCNTs purchased from Applied Nanostructured Solutions LLC. (Baltimore, MD, USA).

### 2.2 Synthesis of photo-polymeric nanocomposites

Nanocomposite resins were prepared by varying MWCNT concentrations (0.01, 0.025, 0.05, 0.1, 0.2, 0.3 phr). As shown in Fig. 1, probe sonication and magnetic stirring were used to disperse MWCNTs. The general procedure involves adding the MWCNTs and 2.5 phr TPO in TPGDA (50 phr). The mixture was probe-sonicated and magnetically stirred simultaneously for eight minutes at 35 Hz frequency with a pulse duration of 5 s (ON) and pulse interval of 15 s (OFF) to avoid excessive heating. Then, PlasClear (50 phr) was added, and the obtained mixture (MWCNT/PlasClear-TPGDA) was magnetically stirred again for 30 min. The obtained nanocomposite resins are designated as PC-*X*, where *X* denotes the MWCNT concentration in phr (e.g., PC-0.01 with 0.01 phr MWCNTs).

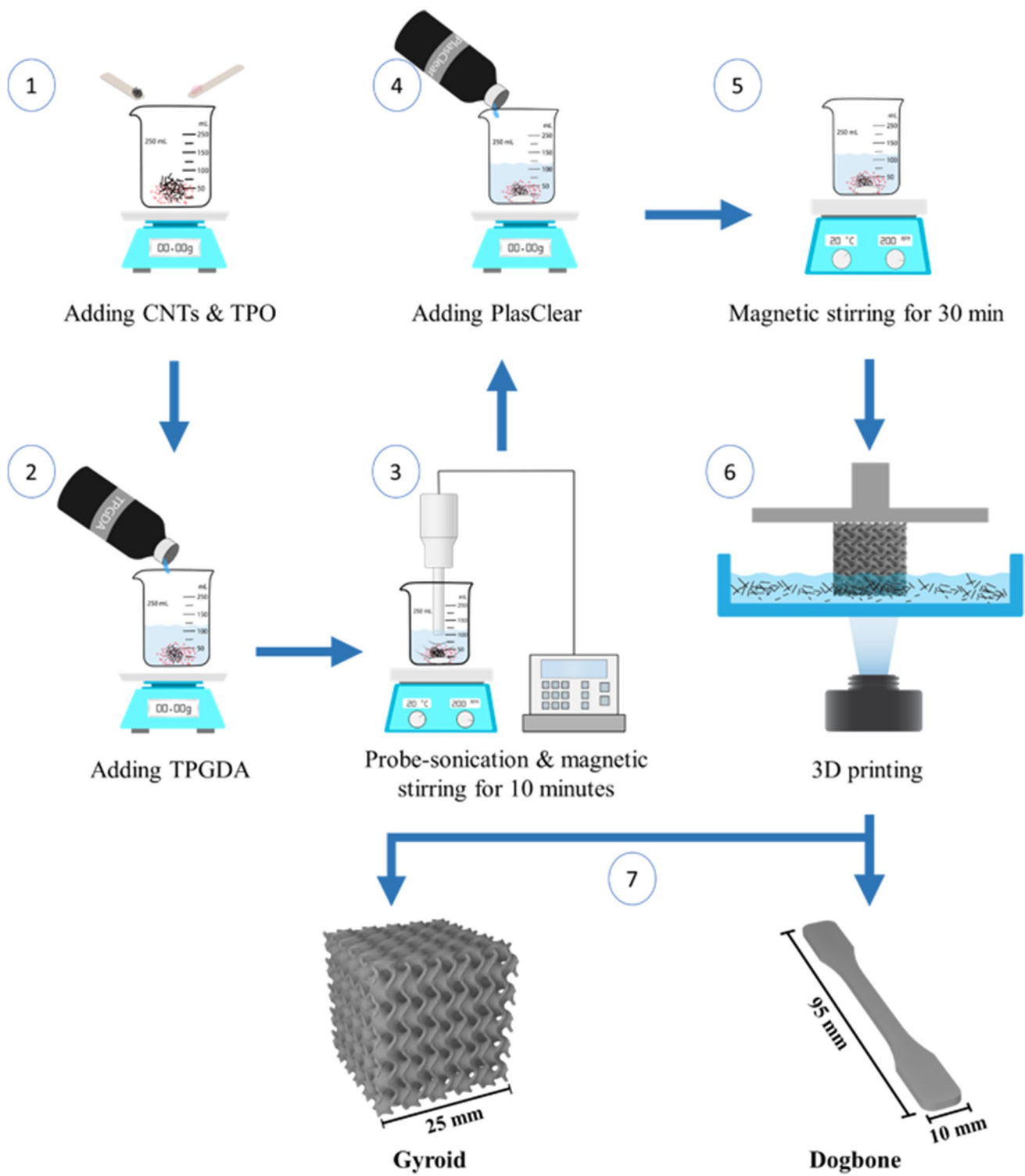


Fig. 1 Schematic diagram showing the manufacturing process consisting of resin preparation (1–5) and DLP 3D printing (6–7)

### 2.3 3D printing of nanocomposites

The Freeform Pro2 DLP (Asiga, Alexandria, Australia) commercial 3D printer was used to print at least three identical

dog-bone shaped standard test specimens for each CNT/resin formulation (gauge section measuring  $33 \times 5 \times 2$  mm according to ASTM 638-type 4) and three identical gyroid lattice structures with 0.05 phr CNT/resin formulation. The gyroid

structure belongs to the family of triply periodic minimal surface (TPMS) lattices and has interconnected porous geometry. The CAD model (Fig. 1) was designed using Matlab according to the governing equation of the gyroid surface:

$$\cos(x)\sin(y) + \cos(y)\sin(z) + \cos(z)\sin(x) = 0 \quad (1)$$

The wall thickness of the gyroid was set to 40  $\mu\text{m}$  to obtain a relative density of 30%.

For all prints, the prepared MWCNT/PlasClear-TPGDA nanocomposite resins (see Section 2.2) were used as the feedstock. The Freeform Pro2 is a bottom-up DLP printer with a 75- $\mu\text{m}$  XY resolution and a 385-nm LED lamp whose UV light is concentrated at the vat's bottom surface to cure a layer of resin between the bottom of the vat and the build platform. For all samples, the exposure time per layer (or slice) was set at 7 s, the slice thickness was set to 50  $\mu\text{m}$ , and the light intensity was 5.20  $\text{mW}/\text{cm}^2$  (unless otherwise stated). To ensure good quality of the printed samples, the MWCNT loading in the liquid resin was limited to 0.05 phr, as further discussed in Section 3.1. After 3D printing, all the specimens were thoroughly rinsed with isopropyl alcohol (IPA) to remove any uncured liquid resin, and then dried in air before storing them in a dark cabinet. Note that UV post-curing was not performed, unless otherwise stated.

## 2.4 Characterization techniques

The electrical resistance of the printed samples (30 mm  $\times$  5 mm  $\times$  2 mm) was measured using a Tektronix 6.5-digit DMM 4050 multimeter. The bulk resistivity was calculated using a two-point probe method according to ASTM B193. The resistivity of the printed sample was determined using

$$\rho = \frac{RA}{l} \quad (2)$$

where  $R$  is the measured resistance,  $A$  is the cross-sectional area of the sample, and  $l$  is the distance between the probes.

A SVM 3000 stabinger viscometer (Anton Paar, Austria) was used to measure the viscosities of the as-prepared nanocomposite resins. The tests were conducted at room temperature (25  $^{\circ}\text{C}$ ) using ASTM D7042 standard. SEM was used to analyze the microstructure of MWCNT nanocomposites. Cross-sectional images of cryogenically fractured 3D printed nanocomposites were acquired using a scanning electron microscope (Nova NanoSEM 650, FEI Co., USA) with 7.5–10 kV accelerating voltage. A thin layer of Au (8 nm) was sputtered on the nanocomposite specimens to ensure good quality, high resolution images.

3D printed nanocomposite specimens were subjected to thermogravimetric analysis (TGA) using a SDT Q600

instrument (TA Instruments, New Castle, USA) between 25 and 500  $^{\circ}\text{C}$  in  $\text{N}_2$  atmosphere to examine the thermal stability of the samples according to ASTM E1131. The heating rate was set to 10  $^{\circ}\text{C}/\text{min}$  in all experiments. In addition, differential scanning calorimetry (DSC) was conducted as per ASTM standard E1356 using a DSC131 EVO instrument (Setaram Inc, Lyon, France) over a temperature range of 25–200  $^{\circ}\text{C}$  at a heating rate of 10  $^{\circ}\text{C}/\text{min}$  to investigate the glass transition temperature ( $T_g$ ) and curing enthalpy ( $\Delta H_{\text{cure}}$ ) of the 3D printed (solid) and uncured (liquid) resins. The  $T_g$  was measured by the extrapolated onset temperature of the glass transition (i.e., intersection point of the baseline tangent with the inflectional tangent of the glass transition), and the curing enthalpy was determined by the area under the observed peak.

A Zwick-Roell universal testing machine (UTM) with a 2.5 kN load cell was used for all the mechanical tests performed in this study. Monotonic tensile tests were performed on the 3D printed dogbone specimens (see Section 2.3) to evaluate the mechanical properties of the nanocomposites with different CNT concentrations. The standard used was ASTM D638. The crosshead speed was maintained at 2.5 mm/min for all samples, and the elongation of the specimen was obtained from the cross-head displacement of the UTM (assuming that all deformation occurs in the gauge section of the specimen). During the tensile test, the change in electrical resistance,  $\Delta R = R - R_0$ , was measured in situ using a Tektronix 6.5-digit DMM 4050 multimeter (measuring range between 0.01  $\Omega$  and 1000  $\text{M}\Omega$ ), where  $R$  represents the actual resistance of the test specimen at strain  $\varepsilon > 0$  and  $R_0$  denotes the no-load resistance corresponding to  $\varepsilon = 0$ . The gauge factor,  $k$ , determines the piezoresistive sensitivity of the material and is defined as follows:

$$k = \frac{\Delta(\Delta R/R_0)}{\Delta\varepsilon} \quad (3)$$

where  $\Delta R/R_0$  is the normalized resistance change occurring over a strain increment  $\Delta\varepsilon$ , and  $R_0$  is the no-load resistance. Note that the multimeter probes were connected to a copper tape attached between the specimen and the insulated grips of the UTM, as shown in the Fig. S8 (Supplementary Material). The multimeter readings were then transferred to a computer and synchronized with the force–displacement data of the UTM. At least three repeated tests were performed on virgin specimens to confirm the repeatability of the measurements.

In addition, uniaxial compression tests were performed on the 3D printed gyroid structure (cross-head speed 2.5 mm/min) to study its collapse response under large compressive strains. The strain- and damage-sensing capability of the structure was assessed by measuring the resistance change,  $\Delta R$ , during the test, as described above. Here, thin copper

sheets (0.50 mm thick) were placed between the specimen and the insulated loading fixture of the UTM which served as electrodes for the resistance measurements.

The cyclic response of the 3D printed nanocomposites was measured under fluctuating tensile loads using the same techniques as in the monotonic tensile tests described above. Two test protocols were considered as follows.

### 2.4.1 Strain-controlled cyclic loading

The sample was monotonically loaded up to a maximum strain of  $\epsilon = 1\%$  and then immediately unloaded (without holding time) to  $\epsilon = 0.3\%$  at a cross-head speed of 2.5 mm/min. These load-unload cycles were repeated 10 times to examine the stability of the material’s strain sensing functionality over repetitive strain cycles. Here, the strain amplitudes were chosen low to ensure that the response was predominantly elastic. Moreover, we note that the specimens were unloaded to a non-zero strain (0.3%) to avoid the occurrence of compressive stresses as a result of viscoelastic damping.

### 2.4.2 Incremental cyclic loading

The sample was subject to five load–unload cycles in which the strain amplitude was increased incrementally (1%, 2.5%, 4%, 5.5%, and 7%) to examine the effect of inelastic deformation on the sensing performance of the nanocomposites. In each of these load cycles, the sample was unloaded to zero stress without holding time. A constant cross-head speed of 2.5 mm/min was used for all load–unload cycles.

## 3 Results and discussion

### 3.1 Effect of CNT loading on the resin viscosity and conductivity of 3D printed samples

The addition of MWCNTs to the photopolymer can drastically increase the resin’s viscosity and affect the recoating of

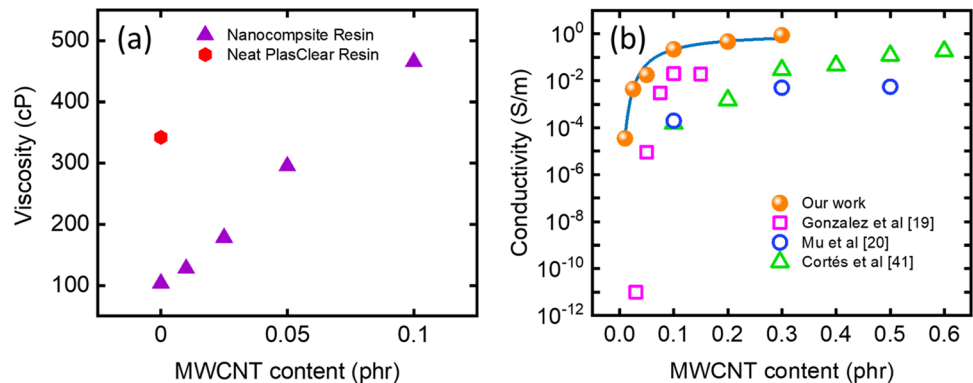
layers during 3D printing, creating a large amount of voids and cavities in the printed parts and leading to failed prints. Hence, it is necessary to examine the effect of MWCNT loading on the resin’s viscosity. Figure 2a presents the measurements of the apparent resin viscosity at room temperature as a function of MWCNT content, showing a nearly linear increase in viscosity with increasing MWCNT loading. Note that the data points in Fig. 2a represent the averages of two repeated tests, and since the two readings for each sample were almost identical, the error bars were omitted. Without the addition of MWCNTs, our resin had a viscosity of 103.9 mPa·s (see Table 1), which was much lower than that of the commercial PlasClear resin (see red circle in Fig. 2a), thanks to the addition of 50 phr TPGDA, which acted as a reactive diluent. As a result, after adding 0.05 phr of MWCNTs, the resin’s viscosity (294.9 mPa·s) was still lower than that of the neat PlasClear resin (see Fig. 2a), which resulted in high-quality DLP prints with negligible porosity, as seen from  $\mu$ -CT images of the printed samples (see Fig. S1, Supplementary Material). It is important to note that resins with CNT loadings  $\geq 0.1$  phr required a longer curing time for printing ( $> 7$  s per layer). Hence, we only consider nanocomposite with CNT loadings up to 0.05 phr in the following to ensure that the processing conditions are identical for all compositions.

The effect of MWCNT concentration on the electrical conductivity of 3D printed samples was also investigated,

**Table 1** Viscosity values for MWCNT/resin mixtures with different MWCNT contents measured at room temperature

CNT content (phr)	Resin formulation (ratio)		Dynamic viscosity (mPa·s)
	PlasClear	TPGDA	
0	1	0	342
0	1	1	103.9
0.01	1	1	128.0
0.025	1	1	178.2
0.05	1	1	294.9
0.1	1	1	465.3

**Fig. 2** **a** Dynamic viscosities of the uncured nanocomposite resins (purple triangles) and the commercial PlasClear resin (red circle); **b** electrical conductivity of the 3D printed nanocomposites as a function of MWCNT content compared with similar photoresins used in DLP technique



and the results are shown in Fig. 2b, along with the values reported in the literature for similar DLP 3D printed materials. The blue curve in the figure represents a three-parameter exponential curve fitted using Origin software [42]. When the MWCNT concentration was less than 0.01 phr, the nanocomposite was considered non-conductive since the sample's resistance exceeded the instrument's limit (1000 M $\Omega$ ). At a nanofiller loading between 0.01 and 0.1 phr, the electrical conductivity increased by four orders of magnitude, reaching 0.219 S/m at 0.1 phr, indicating that electrical percolation had commenced, as seen from Fig. 2b. When the CNT concentration was further increased to 0.3 phr, the conductivity increased more modestly to 0.875 S/m. These trends are similar compared to those reported in previous studies [19, 20, 41], but the electrical conductivity of our 3D printed nanocomposites is significantly higher even at lower concentrations of CNTs, possibly due to more uniform

dispersion of MWCNTs in our samples. In this study, the MWCNTs were dispersed through simultaneous probe sonication and magnetic stirring (see Fig. 1), which differed from the dispersion techniques used in previous studies, such as three-roll milling [20, 41] or sonication at low intensity [19].

### 3.2 Microstructure analysis

Figure 3 shows SEM images of the 3D printed nanocomposites with MWCNT loading of 0.01 phr (top row), 0.025 phr (middle row), and 0.05 phr (bottom row). The images show the cross-section of cryogenically fractured samples. For MWCNT loadings up to 0.025 phr, the MWCNTs appear to be well-dispersed and can be noticed protruding out of the fracture surface, indicating that they were pulled out of the polymer matrix during the fracture process as a result of weak interfacial bonding. While the energy dissipated during pull-out of the

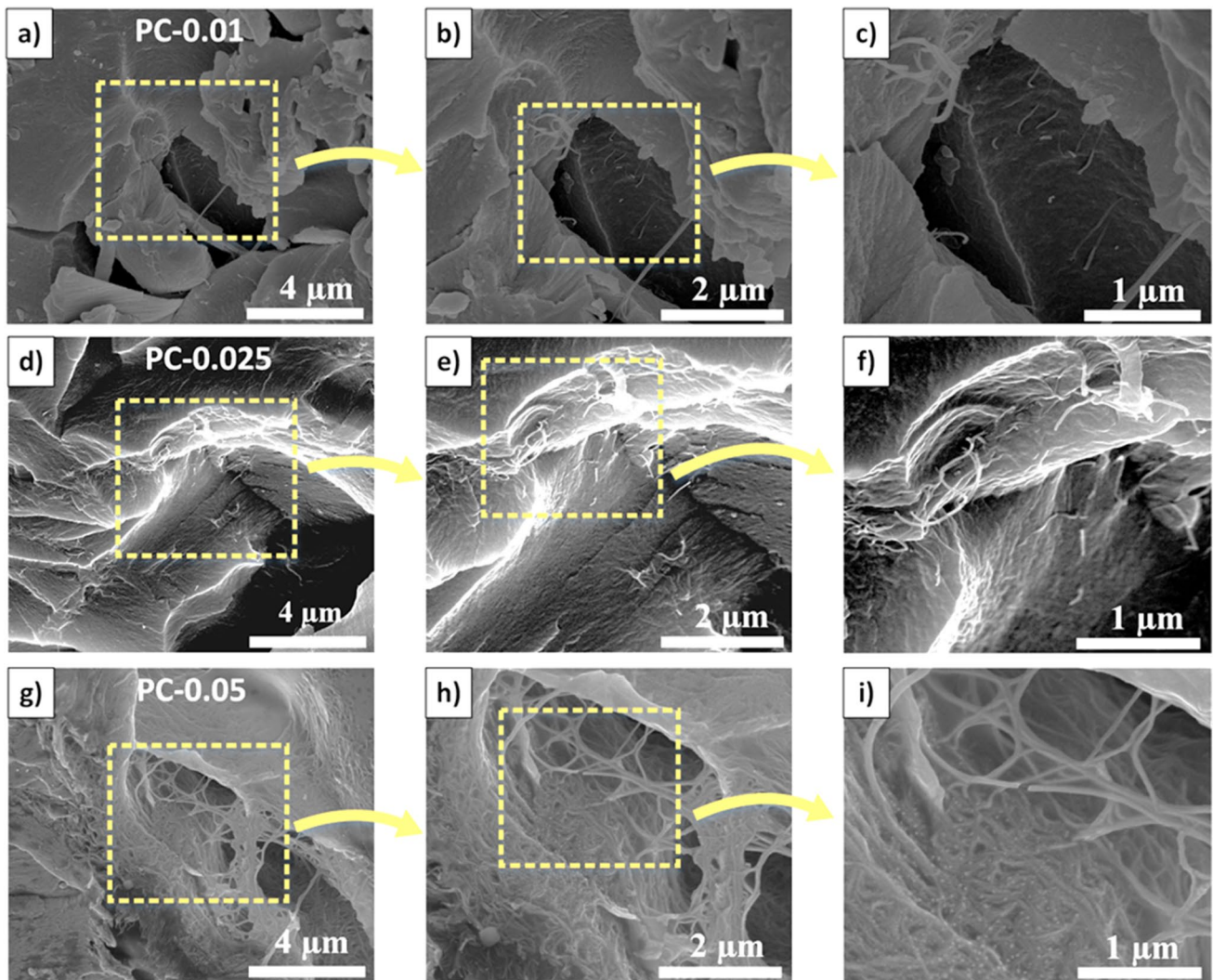


**Fig. 3** SEM images of DLP 3D printed nanocomposites with different MWCNT concentrations: **a–c** 0.01 phr; **d–f** 0.025 phr; **g–i** 0.05 phr

CNTs could help to increase the toughness of the nanocomposite, the MWCNT content is too low to significantly affect the fracture behavior (see Section 3.4.2). As expected, the amount of MWCNTs seen in the images increases as the MWCNT loading increases. For the PC-0.05 nanocomposite, we observe agglomeration of MWCNTs in the form of bundles, a morphology similar to that observed in the as-received MWCNTs (see Fig. S2, Supplementary Material).

### 3.3 Thermal characterization

#### 3.3.1 Differential scanning calorimetry

DSC curves of uncured (liquid) neat resin and the 3D printed (solid) nanocomposites are shown in Fig. 4a. The curing enthalpy,  $\Delta H_{\text{cure}}$ , and glass transition temperature,  $T_g$ , evaluated from these curves are listed in Table 2. The value of  $T_g$  decreases steadily with increasing MWCNT loading, which can be explained by the UV shielding effect of the embedded nanofillers, resulting in reduced curing of the nanocomposites and a decrease in cross-link density [43]. A reduction in cross-linking with increasing nanofiller content was also noticed by the difference in curing enthalpy ( $\Delta H_{\text{cure}}$ ) of the printed specimens. For the uncured resin, the onset of curing was found to be at  $\sim 190$  °C, which was not noticed in the neat polymer sample. However, the MWCNT/polymer nanocomposites showed curing enthalpy peaks in the range of 190–220 °C, with the curing enthalpy increasing with the CNT concentration (see Table 2). This is an indication of incomplete curing of the 3D printed nanocomposite specimens due to the UV shielding effect of the nanofillers, as reported in previous studies [41, 44, 45]. The UV shielding effect of MWCNTs refers to their ability to absorb UV radiation because they have energy levels that match the energy of UV photons. When a UV photon is absorbed by a MWCNT, it is absorbed and re-emitted as a lower energy

**Table 2** DSC and TGA results for uncured neat resin, as well as 3D printed neat polymer and MWCNT/polymer nanocomposites

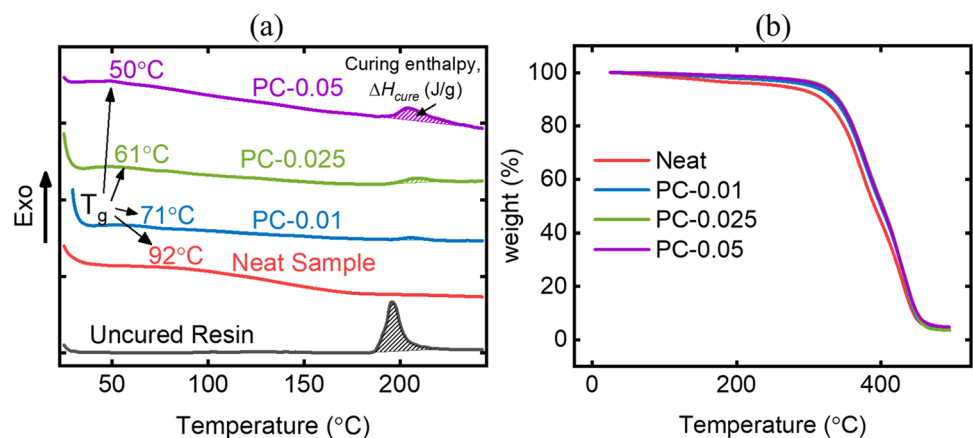
	$T_g$ (°C)	$\Delta H_{\text{cure}}$ (J/g)	$T_{0.1}$ (°C)	$T_{0.5}$ (°C)
Uncured resin	-	-363	-	-
Neat specimen	92.3	-	330	391
PC-0.01	71.1	-27.7	332	400
PC-0.025	61	-29.1	334	401
PC-0.05	50.4	-61	336	402

photon, resulting in the photoinitiator to absorb less UV radiation [44, 45]. Note that the photoinitiators absorb light in the UV spectral range, generally 250–450 nm. It is essential to mention here that the printing parameters for all of the specimens were kept constant.

#### 3.3.2 Thermogravimetric analysis

Non-isothermal decomposition trends of the 3D printed nanocomposites are shown in Fig. 4b. While three virgin specimens were analyzed for each concentration, only one was included in Fig. 4b, since they all showed similar trends. All the printed specimens degraded in a single stage between 320 and 450 °C. The onset temperature of degradation,  $T_{0.1}$ , was found by the intersection of a tangent at the maximum slope and a tangent at the minimum slope of each TGA curve, while the midpoint degradation temperature,  $T_{0.5}$ , corresponds to 50% weight loss on the TGA curve. The  $T_{0.1}$  and  $T_{0.5}$  results are included in Table 2, where each value represents the average of three repeated tests. The results show that both  $T_{0.1}$  and  $T_{0.5}$  increased slightly with increasing MWCNT loading. The embedded MWCNTs possess high thermal stability and restrict the molecular mobility of the polymer near the interface, delaying the thermal degradation process.

**Fig. 4** a DSC and b TGA curves of uncured liquid resin, as well as 3D printed neat polymer and MWCNT/polymer nanocomposites with 0.01, 0.025, and 0.05 phr MWCNT loading



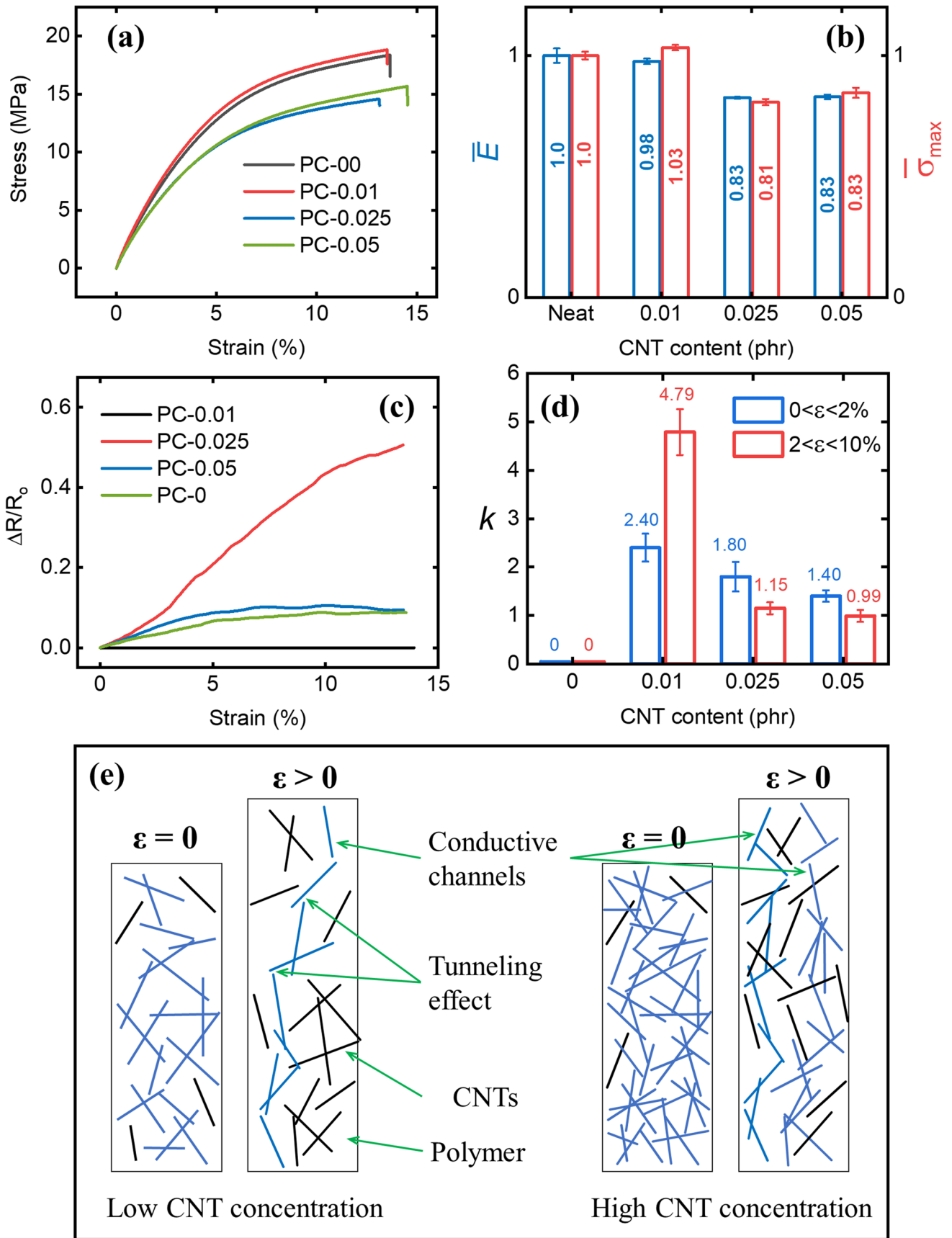


**Fig. 5** Mechanical and piezoresistive behavior of DLP-enabled nanocomposites with various MWCNT concentrations under uniaxial tension: **a** stress vs. strain response; **b** normalized Young's modulus and ultimate strength; **c** normalized resistance change as a function of applied strain; **d** gauge factors evaluated for two strain ranges; **e** graphical representation of CNT/polymer nanocomposite with different concentrations of CNTs subject to tensile loading

### 3.4 Mechanical and piezoresistive response of 3D printed nanocomposites

#### 3.4.1 Monotonic tensile loading

Figure 5a shows typical stress ( $\sigma$ ) vs. strain ( $\epsilon$ ) responses of the 3D printed nanocomposites measured under monotonic tensile loading. The corresponding values of normalized Young's modulus,  $\bar{E} = E/E_0$ , and ultimate tensile strength,  $\bar{\sigma} = \sigma_T/\sigma_{T0}$ , are plotted in Fig. 5b, noting that  $E_0$  and  $\sigma_{T0}$  denote Young's modulus and tensile strength of the neat PC-0. The  $E$  and  $\sigma_T$  values for each nanocomposite are listed in Table 3. Initially, the stress–strain curves show linear trends, but these become increasingly nonlinear at  $\epsilon > 2\%$ . The observed nonlinearities can be ascribed to the occurrence of viscoelastic/viscoplastic deformation during the tensile tests. Note that the viscoelastic behavior of the 3D printed nanocomposites was confirmed by the results of our dynamic mechanical analysis (DMA), showing that the PlasClear-TPGDA matrix exhibits a loss factor,  $\tan \delta > 0.1$  at room temperature (see Fig. S3, Supplementary Material). It is also seen in Fig. 5a–b that the response of the nanocomposite with 0.01 phr MWCNT loading (PC-0.01) is very similar to that of the neat PC-0. A further increase in the MWCNT concentration resulted in a reduction of tensile strength and Young's modulus of about 20%, respectively (see Fig. 5b). With the addition of MWCNTs, a larger portion of the UV light is absorbed by the nanofillers, which decreases the rate of cross-linking in the polymer during 3D printing (as detailed in Section 3.3.1) and therefore reduces its strength and modulus, in line with the findings of previous studies [41]. Although the addition of CNTs can limit polymer chain mobility, this effect is outweighed by the existence of insufficiently cured resin in the nanocomposites, which enhances molecular movement. Note that by reducing the layer thickness in DLP 3D printing or by using post-treatments (e.g., UV post-curing, thermal annealing), a highly cured polymer with enhanced strength and modulus can be obtained, as discussed in the Supplementary Material (see Sections S3 and S4). Furthermore, it is observed from Fig. 5a that all the nanocomposites show a similar strain tolerance, exhibiting failure strains within a narrow range of 13–15%. Since yield points cannot be clearly identified from the stress–strain curves, we used the 0.1% strain offset method to evaluate the yield strength, reporting 5.9, 6.3, 4.1, and

4.1 MPa for 0, 0.01, 0.025, and 0.05 phr MWCNT loading, respectively.

The addition of MWCNTs to the PlasClear-TPGDA matrix not only altered the mechanical response but also imparted piezoresistive strain sensing functionality to the printed nanocomposites. With the application of load, the conductive nanofillers in the percolating network move apart and begin to align in the direction of loading, causing relatively high changes in electrical resistance. This is demonstrated in Fig. 5c where the normalized change in resistance,  $\Delta R/R_0$ , is plotted against the applied tensile strain,  $\epsilon$ , while the corresponding gauge factors are shown in Fig. 5d for each composition.

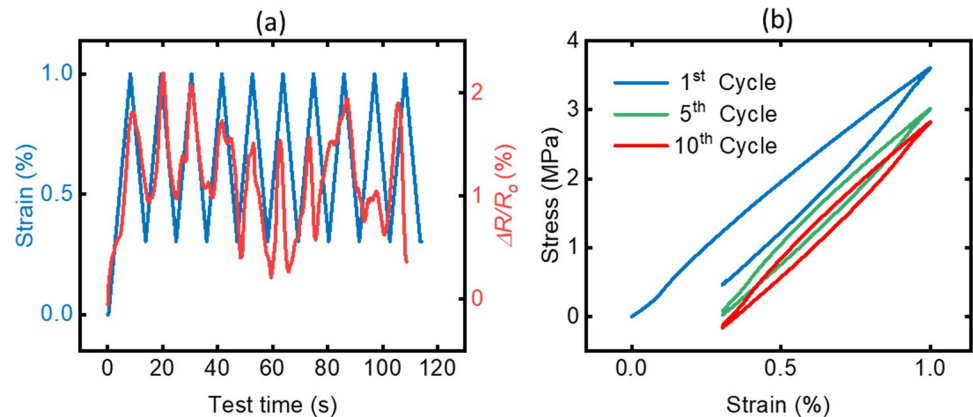
For each curve in Fig. 5c, two gauge factor values were evaluated, one in the initial linear-elastic regime (taken as  $0 \leq \epsilon \leq 2\%$ ) and the other in the inelastic regime (taken as  $2 \leq \epsilon \leq 10\%$ ), as shown in Fig. 5d. Over both elastic and inelastic regimes, the nanocomposite with the lowest nanofiller loading (i.e., PC-0.01) showed the greatest change in resistance (see Fig. 5c). For the PC-0.01, PC-0.025, and PC-0.05, the  $\Delta R/R_0$  values at  $\epsilon = 2\%$  strain were 2.4%, 1.8%, and 1.5%, respectively, and at the fracture point, these values increased to 50%, 9.4%, and 8.7%. The higher sensitivity of the nanocomposites with lower MWCNT loading can be explained with the help of Fig. 5e, where deformation-induced changes in the morphology of the percolating network are schematically illustrated for the case of low and high CNT loading, respectively. The application of a tensile load on the nanocomposite causes the CNTs in the percolating network to move apart, resulting in a break-down of electron conduction in some branches of the network when the inter-tube distance exceeds the effective distance for electron tunneling (typically 1–2 nm [46]). At lower CNT loading (i.e., slightly above the percolation threshold), the average distance between the CNTs is expected to be higher, causing some conductive channels in the network to get cutoff at lower macroscopic strains, yielding higher changes in resistance. This mechanism has been studied extensively and is reported in several studies [47–50].

#### 3.4.2 Cyclic loading

Low-amplitude cyclic tests were performed on the 3D printed nanocomposites to examine the stability of their strain sensing characteristics in the elastic regime when subject to repeated strain cycles in tension. Figure 6a presents the time histories of the applied strain along with the measured resistance changes,  $\Delta R/R_0$ , while the corresponding stress vs. strain loops recorded for the 1st, 5th, and 10th cycle are plotted in Fig. 6b. Since all nanocomposites showed similar resistance changes in the elastic regime (see Fig. 5d), only the results for the PC-0.05 nanocomposite are discussed here (similar

**Table 3** Summary of mechanical and piezoresistive properties of the 3D printed nanocomposites

	Elastic modulus (MPa)	Yield strength (MPa)	Ultimate tensile strength (MPa)	Gauge factor ( $0 < \varepsilon < 2\%$ )	Gauge factor ( $2 < \varepsilon < 10\%$ )
Neat	315.6	5.9	18.2	0	0
PC-0.01	308	6.3	18.8	2.40	4.79
PC-0.025	260.6	4.1	14.7	1.80	1.15
PC-0.05	261.7	4.1	15.4	1.40	0.99

**Fig. 6** Strain-controlled cyclic tensile loading of PC-0.05 nanocomposite with constant strain amplitudes: **a** time histories of applied strain (blue) and normalized change in resistance (red); **b** stress vs. strain responses measured for the 1st, 5th and 10th load cycles

results for the PC-0.025 can be found in section S5, Supplementary Material). As seen from Fig. 6a, the resistance of the nanocomposite increases when stretched and reduces when unloaded, but the piezoresistive response of the material changes in each load cycle. This behavior can be explained by the occurrence of stress relaxation in the nanocomposite during the test resulting from its viscoelastic behavior, as discussed in the DMA section (see section S2, Supplementary Material). When the material is stretched, the distances between adjacent CNTs in the percolating network increase, causing the tunneling resistance, and hence the network resistance to increase. When the material is unloaded, some of the CNTs do not return immediately to their original positions, due to the viscoelastic nature of the polymer matrix that separates them, altering the piezoresistivity of the network in the following load cycle. Although this behavior makes it difficult to determine the actual strain level in repeated load cycles, these nanocomposites can still be useful for internal sensing of vibrations or overloads during service. The aforementioned stress relaxation behavior is also evident from the observed decrease in the peak stress between two consecutive load cycles (decrease in mean stress) and the pronounced hysteresis loops seen in the stress–strain curves (see Fig. 6b). It is also worth noting that the area of the hysteresis loops, and hence, the energy dissipated in a load cycle, decreases with increase in the number of cycles, although the difference in energy dissipation between the 5th and 10th cycles is not significant. Moreover, strain-controlled constant amplitude repetitive cyclic

tests indicate that the secant elastic modulus decreases in PC-0.05 nanocomposite, while the maximum strain imposed is less than the yield strain.

The cyclic mechanical and piezoresistive response of the PC-0.05 nanocomposite under incrementally growing strain amplitudes is presented in Fig. 7. Here, the maximum and minimum values of  $\Delta R/R_0$  (corresponding to the maximum and minimum strain imposed) continued to rise in subsequent cycles (see Fig. 7a), as a result of the growing strain amplitudes and concomitant accumulation of inelastic strains upon unloading (see Fig. 7b). It shows that the plastic strains induced beyond the yield point cause permanent changes in the percolating CNT network, resulting from the plastic deformation and possible damage (e.g., micro-cracks) in the surrounding polymer matrix and the deformation/re-orientation of the embedded CNTs. We also observe, from Fig. 7c, that the  $\Delta R/R_0$  vs. strain response acquired for each load cycle is markedly different between loading and unloading cycles. Furthermore, we observe that the loading curves do not follow the same trends as their previous unloading curves, and similar trends exist in the stress vs. strain curves (see Fig. 7b). Since unloading is an elastic process, these differences most likely stem from the viscoelastic behavior of the nanocomposite, preventing the CNTs to return to a fully relaxed state upon unloading [50]. The residual strain upon unloading,  $\varepsilon_r$ , and the corresponding change in resistance  $\Delta R_r/R_0$  are plotted in Fig. 7d for each load cycle. It is clear from the figure that  $\Delta R_r/R_0$  increases steadily with increasing  $\varepsilon_r$ , as a result of the permanent changes in the percolating network by matrix yielding and damage as well

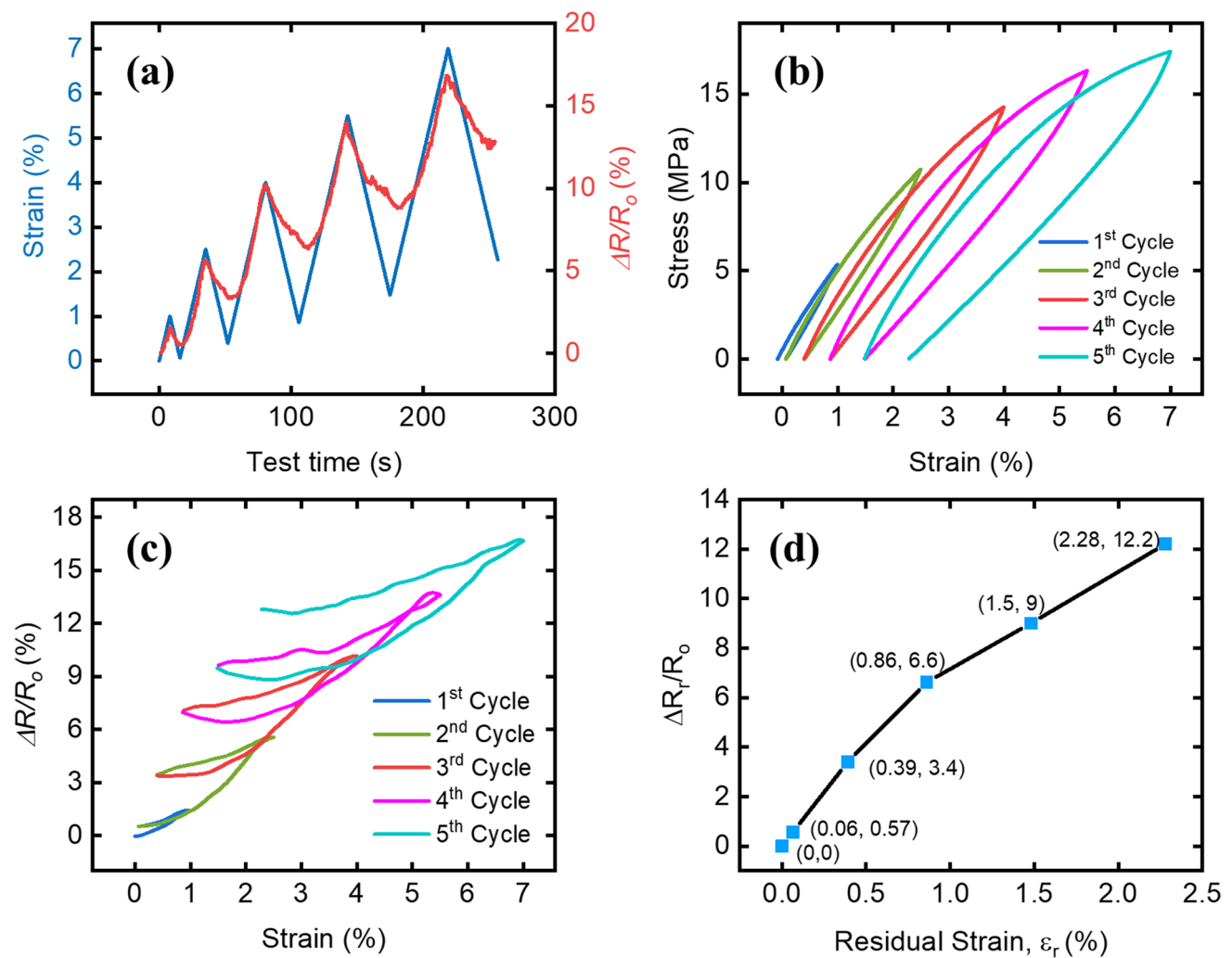


**Fig. 7** Cyclic tensile loading of PC-0.05 nanocomposite with incrementally growing strain amplitudes: **a** time histories of applied strain and normalized change in resistance; **b** stress vs. strain responses;

**c** normalized resistance change plotted against strain, **d** normalized resistance changes measured at the residual strain upon unloading in each cycle

as CNT re-orientation. For practical applications, the latter curve can be useful in identifying unexpected overloads in service or detecting the occurrence of damage in a structure following an accident.

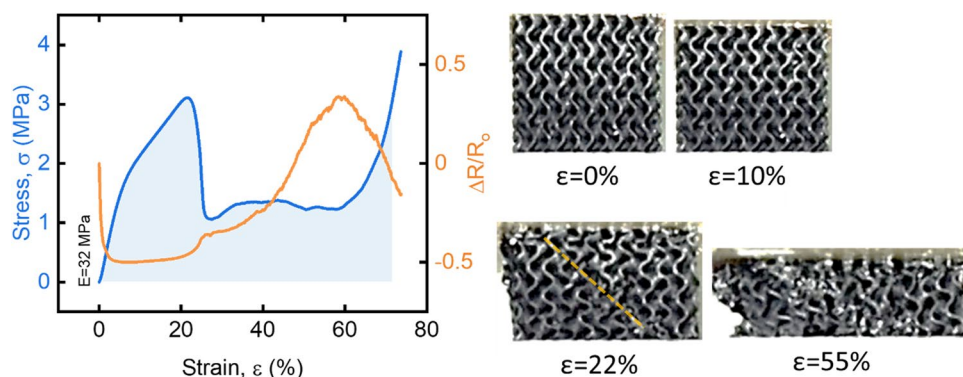
### 3.5 Mechanical and piezoresistive behavior of a self-sensing gyroid lattice

Having studied the mechanical and piezoresistive behavior of the 3D printed MWCNT/PlasClear-TPGDA nanocomposites, we now demonstrate their self-sensing functionality for the case of a 3D printed gyroid lattice. Figure 8 shows the compressive stress vs. strain response for a gyroid lattice printed using PC-0.05 with a relative density of 30%; we also include the corresponding  $\Delta R/R_0$  vs. strain curve measured in situ during the compression tests along with

an image sequence showing the deformation mechanism of the structure.

Initially, the stress increases linearly with strain until the yield point is reached at  $\epsilon \approx 10\%$ , beyond which the stress continues to increase with strain at a more moderate rate. At  $\epsilon \approx 22\%$ , the structure starts to collapse and the stress drops sharply. During this phase, we observe the formation of a diagonal crush band in the structure, triggered by brittle fracture of the cell walls. Subsequently, the structure continues to crush at a nearly constant stress of  $\approx 1$  MPa until densification commences at  $\epsilon \approx 55\%$ , which is associated with a steep increase in the slope of the stress–strain curve. The piezoresistive functionality imparted to the structure by the addition of CNTs helps in monitoring the deformation and damage state of structure [51], as discussed in the following. During the initial (elastic) phase of the response, we observe a sharp decrease in  $\Delta R/R_0$  with a gauge factor value of 20 as the

**Fig. 8** Uniaxial compressive stress vs. strain response of a DLP-enabled MWCNT/polymer gyroid lattice (30% relative density) along with the measured piezoresistive response; the images show photographs of the specimen recorded during the test at various strain levels



CNTs move closer to each other within the cell walls, increasing the conductivity of cell wall material. This is followed by a short plateau in which  $\Delta R/R_0$  slightly increases, possibly due to micro-scale yielding and failure processes occurring locally at printing imperfections in the walls of the gyroid. A noticeable increase in  $\Delta R/R_0$  is observed near the collapse point when some of the walls of the gyroid structure start to collapse suddenly (i.e., due to destruction of conductive paths resulting from collapse of cell walls). During the subsequent collapse phase, we observe a nearly linear increase in  $\Delta R/R_0$  with increasing strain, due to the formation of additional steady crush bands in the structure, causing further breakdown of conductive channels in the CNT network. The latter trend is reversed at the onset of densification, where percolation of contacts between fractured walls of the gyroid commences, facilitating new pathways for electron transfer. The observed piezoresistive characteristics correspond well with the different regimes of deformation (elasticity, yielding, collapse and densification). In particular, the distinct changes in the slope of the  $\Delta R/R_0$  vs. strain curve could be useful in detecting transitions between different deformation regimes, thus providing insight into the damage state of the structure.

## 4 Conclusions

Digital light processing (DLP) was utilized to additively manufacture electrically conductive CNT/polymer nanocomposites and smart gyroid lattice structures. By mixing commercially available photoresin (PlasClear) with a reactive diluent (TPGDA), photoinitiator (TPO) and different concentrations of MWCNTs (0.01, 0.025, or 0.05 phr), nanocomposite resins with low viscosity, high conductivity and excellent printability were synthesised. As a result, electrical percolation in the 3D printed samples was achieved at an ultra-low MWCNT loading of 0.01 phr, and their conductivity was significantly higher than those of similar SLA/DLP 3D printed nanocomposites reported in previous studies. The nanocomposite with the lowest nanofiller content (0.01 phr MWCNTs) exhibited

the highest tensile strength and elastic modulus. Increased CNT content resulted in a loss of stiffness and strength, due to the dispersed CNTs shielding some of the UV light and preventing complete curing of the polymer matrix, as confirmed by DSC analysis. Reducing the MWCNT concentration in the nanocomposites also led to higher piezoresistive sensitivity, as a result of the increased inter-tube distances which caused incremental break-down of electron tunneling in some channels of the percolating network at lower strains. At 0.01 phr MWCNT loading, the gauge factor in the initial (elastic) phase of the response was 2.4, which increased to 5.0 beyond the yield point. The sensing performance of the nanocomposites was also studied under cyclic tensile loading. The measurements revealed differences in the piezoresistive behavior between consecutive load cycles, which was attributed to the viscoelastic behavior of the nanocomposites (as confirmed via DMA), preventing the CNTs in the percolating network to return to a fully relaxed state upon unloading and therefore altering their piezoresistive behavior in the following load cycle. Finally, the developed resin was used to print a self-sensing gyroid lattice structure, and its strain and damage sensing functionalities were experimentally examined. The piezoresistive response of the gyroid lattice exhibited distinct changes in strain sensitivity at the onset of yielding, collapse and densification, which could be useful in detecting transitions between different deformation regimes, thus providing insight into the damage state of the structure. The results of this study suggest that DLP is a promising 3D printing technique for creating novel self-sensing multifunctional systems with complex geometries at ultra-low nanofiller loading. Furthermore, the use of more flexible/stretchable resins could be attractive for the fabrication of micro-architected sensors and electrodes, which is anticipated to advance research in the field of wearable electronics moving forward.

**Supplementary Information** The online version contains supplementary material available at <https://doi.org/10.1007/s00170-023-11123-8>.

**Author contribution** Conceptualization: S. Kumar, A. Schiffer; investigation: O.W. Saadi; data curation: O.W. Saadi; visualization: O.W. Saadi; writing — original draft preparation: O.W. Saadi; writing — review and editing: A. Schiffer, S. Kumar; resources: S. Kumar, A. Schiffer; funding acquisition: S. Kumar, A. Schiffer; project administration: S. Kumar, A. Schiffer.

**Funding** The authors are grateful for the financial support provided by the Khalifa University through the Competitive Internal Research Award (CIRA) 2018 [grant number CIRA-2018–128].

**Data availability** Data will be made available on request.

**Code availability** Not applicable (only commercial software was used).

## Declarations

**Ethics approval** Not applicable.

**Consent to participate** Not applicable.

**Consent for publication** All authors read and agreed to the published version of the manuscript.

**Competing interests** The authors declare no competing interests.

**Open Access** This article is licensed under a Creative Commons Attribution 4.0 International License, which permits use, sharing, adaptation, distribution and reproduction in any medium or format, as long as you give appropriate credit to the original author(s) and the source, provide a link to the Creative Commons licence, and indicate if changes were made. The images or other third party material in this article are included in the article's Creative Commons licence, unless indicated otherwise in a credit line to the material. If material is not included in the article's Creative Commons licence and your intended use is not permitted by statutory regulation or exceeds the permitted use, you will need to obtain permission directly from the copyright holder. To view a copy of this licence, visit <http://creativecommons.org/licenses/by/4.0/>.

## References

1. Bagheri A, Jin J (2019) Photopolymerization in 3D printing. *ACS Appl Polym Mater* 1(4):593–611. <https://doi.org/10.1021/acsapm.8b00165>
2. Saroia J et al (2020) A review on 3D printed matrix polymer composites: its potential and future challenges. *Int J Adv Manuf Technol* 106(5–6):1695–1721. <https://doi.org/10.1007/s00170-019-04534-z>
3. Pagac M et al (2021) A review of vat photopolymerization technology: materials, applications, challenges, and future trends of 3d printing. *Polymers* 13(4):1–20. <https://doi.org/10.3390/polym13040598>
4. Verma P, Schiffer A, Kumar S (2021) Thermo-resistive and thermo-piezoresistive sensitivity of carbon nanostructure engineered thermoplastic composites processed via additive manufacturing. *Polym Test* 93:106961. <https://doi.org/10.1016/J.POLYM ERTESTING.2020.106961>
5. Eswaramoorthy SD, Ramakrishna S, Rath SN (2019) Recent advances in three-dimensional bioprinting of stem cells. *J Tissue Eng Regen Med* 13(6):908–924. <https://doi.org/10.1002/term.2839>
6. Ansari V, Calore A, Zonderland J, Harings JAW, Moroni L, Bernaerts KV (2022) Additive manufacturing of  $\alpha$ -amino acid based poly(ester amide)s for biomedical applications. *Biomacromolecules* 23(3):1083–1100. [https://doi.org/10.1021/ACS.BIOMAC.1C01417/ASSET/IMAGES/LARGE/BM1C01417\\_0010.JPEG](https://doi.org/10.1021/ACS.BIOMAC.1C01417/ASSET/IMAGES/LARGE/BM1C01417_0010.JPEG)
7. Lopes AJ, MacDonald E, Wicker RB (2012) Integrating stereolithography and direct print technologies for 3D structural electronics fabrication. *Rapid Prototyp J* 18(2):129–143. <https://doi.org/10.1108/13552541211212113/FULL/XML>
8. Espera AH, Ryan J, Dizon C, Valino AD, Advincula RC (2022) Advancing flexible electronics and additive manufacturing. *Jpn J Appl Phys* 61(SE):SE0803. <https://doi.org/10.35848/1347-4065/AC621A>
9. Hauck BC, Ruprecht BR, Riley PC (2022) Accurate and on-demand chemical sensors: a print-in-place ion mobility spectrometer. *Sens Actuators B Chem* 362:131791. <https://doi.org/10.1016/J.SNB.2022.131791>
10. Schneider J, Kumar S (2020) Multiscale characterization and constitutive parameters identification of polyamide (PA12) processed via selective laser sintering. *Polym Test* 86:106357. <https://doi.org/10.1016/J.POLYMERTESTING.2020.106357>
11. Varghese R, Sood P, Salvi S, Karsiya J, Kumar D (2022) 3D printing in the pharmaceutical sector: advances and evidences. *Sensors Int* 3:100177. <https://doi.org/10.1016/J.SINTL.2022.100177>
12. Ubaid J, Wardle BL, Kumar S (2020) Bioinspired compliance grading motif of mortar in nacreous materials. *ACS Appl Mater Interfaces* 12(29):33256–33266. [https://doi.org/10.1021/ACSAMI.0C08181/SUPPL\\_FILE/AM0C08181\\_SI\\_002.AVI](https://doi.org/10.1021/ACSAMI.0C08181/SUPPL_FILE/AM0C08181_SI_002.AVI)
13. Gupta V, Alam F, Verma P, Kannan AM, Kumar S (2021) Additive manufacturing enabled, microarchitected, hierarchically porous polylactic-acid/lithium iron phosphate/carbon nanotube nanocomposite electrodes for high performance Li-Ion batteries. *J Power Sources* 494:229625. <https://doi.org/10.1016/J.JPOWSOUR.2021.229625>
14. Bauhofer W, Kovacs JZ (2009) A review and analysis of electrical percolation in carbon nanotube polymer composites. *Compos Sci Technol* 69(10):1486–1498. <https://doi.org/10.1016/J.COMPOS CITECH.2008.06.018>
15. Li B, Liang W, Zhang L, Ren F, Xuan F (2022) TPU/CNTs flexible strain sensor with auxetic structure via a novel hybrid manufacturing process of fused deposition modeling 3D printing and ultrasonic cavitation-enabled treatment. *Sens Actuators A Phys* 340:113526. <https://doi.org/10.1016/J.SNA.2022.113526>
16. Deng Y, Li J, He Z, Hong J, Bao J (2020) Urethane acrylate-based photosensitive resin for three-dimensional printing of stereolithographic elastomer. *J Appl Polym Sci* 137(42). <https://doi.org/10.1002/APP.49294>
17. Zheng Y, Huang X, Chen J, Wu K, Wang J, Zhang X (2021) A review of conductive carbon materials for 3d printing: materials, technologies, properties, and applications. *Materials* 14(14). <https://doi.org/10.3390/MA14143911>
18. Mora A, Verma P, Kumar S (2020) Electrical conductivity of CNT/polymer composites: 3D printing, measurements and modeling. *Compos B Eng* 183:107600. <https://doi.org/10.1016/J.COMPOSITESB.2019.107600>
19. Gonzalez G et al (2017) Development of 3D printable formulations containing CNT with enhanced electrical properties. *Polymer (Guildf)* 109:246–253. <https://doi.org/10.1016/J.POLYMER.2016.12.051>
20. Mu Q et al (2017) Digital light processing 3D printing of conductive complex structures. *Addit Manuf* 18:74–83. <https://doi.org/10.1016/J.ADDMA.2017.08.011>
21. Gershoni G, Gercci Y, Dodiuk H, Kenig S, Tenne R (2022) Radiation curing thermosets. *Handbook of thermoset plastics*, pp 891–915. <https://doi.org/10.1016/B978-0-12-821632-3.00012-9>
22. Rallini M, Kenny JM (2017) Nanofillers in polymers. In: *Modification of polymer properties*. Elsevier Inc., pp 47–86. <https://doi.org/10.1016/B978-0-323-44353-1.00003-8>

23. Ma L et al (2021) A 3D flexible piezoresistive sensor based on surface-filled graphene nanosheets conductive layer. *Sens Actuators A Phys* 332:113144. <https://doi.org/10.1016/J.SNA.2021.113144>
24. Lei Z et al (2018) Fabrication of highly electrical conductive composite filaments for 3D-printing circuits. *J Mater Sci* 53(20):14495–14505. <https://doi.org/10.1007/S10853-018-2645-1>
25. Paz R, Moriche R, Monzón M, García J (2020) Influence of manufacturing parameters and post processing on the electrical conductivity of extrusion-based 3D printed nanocomposite parts. *Polymers* 12(4):733. <https://doi.org/10.3390/POLYM12040733>
26. Mohan VB, Krebs BJ, Bhattacharyya D (2018) Development of novel highly conductive 3D printable hybrid polymer-graphene composites. *Mater Today Commun* 17:554–561. <https://doi.org/10.1016/J.MTCOMM.2018.09.023>
27. Kwok SW et al (2017) Electrically conductive filament for 3D-printed circuits and sensors. *Appl Mater Today* 9:167–175. <https://doi.org/10.1016/J.APMT.2017.07.001>
28. Tan JC, Low HY (2018) Embedded electrical tracks in 3D printed objects by fused filament fabrication of highly conductive composites. *Addit Manuf* 23:294–302. <https://doi.org/10.1016/J.ADDMA.2018.06.009>
29. AlMahri S, Schneider J, Schiffer A, Kumar S (2022) Piezoresistive sensing performance of multifunctional MWCNT/HDPE auxetic structures enabled by additive manufacturing. *Polym Test* 114:107687. <https://doi.org/10.1016/J.POLYMTESTING.2022.107687>
30. Borrello J, Nasser P, Iatridis JC, Costa KD (2018) 3D printing a mechanically-tunable acrylate resin on a commercial DLP-SLA printer. *Addit Manuf* 23(August):374–380. <https://doi.org/10.1016/j.addma.2018.08.019>
31. Valencia LM, Herrera M, de la Mata M, de León AS, Delgado FJ, Molina SI (2022) Synthesis of silver nanocomposites for stereolithography: in situ formation of nanoparticles. *Polymers* 14(6):1168. <https://doi.org/10.3390/POLYM14061168>
32. Sanders P et al (2019) Stereolithographic 3D printing of extrinsically self-healing composites. *Sci Rep* 9(1):1–6. <https://doi.org/10.1038/s41598-018-36828-9>
33. Manapat JZ, Chen Q, Ye P, Advincula RC (2017) 3D printing of polymer nanocomposites via stereolithography. *Macromol Mater Eng* 302(9):1–13. <https://doi.org/10.1002/mame.201600553>
34. Lin D et al (2015) 3D stereolithography printing of graphene oxide reinforced complex architectures. *Nanotechnology* 26(43):434003. <https://doi.org/10.1088/0957-4484/26/43/434003>
35. Scordo G et al (2019) A novel highly electrically conductive composite resin for stereolithography. *Mater Today Commun* 19(November 2018):12–17. <https://doi.org/10.1016/j.mtcomm.2018.12.017>
36. Sciancalepore C, Moroni F, Messori M, Bondioli F (2017) Acrylate-based silver nanocomposite by simultaneous polymerization–reduction approach via 3D stereolithography. *Compos Commun* 6(June):11–16. <https://doi.org/10.1016/j.coco.2017.07.006>
37. Chantapanich N, Puttawibul P, Sitthiseripratip K, Sucharitpawatskul S, Chantaweroad S (2013) Study of the mechanical properties of photo-cured epoxy resin fabricated by stereolithography process. *Songklanakar J Sci Technol* 35(1):91–98
38. Chiappone A et al (2016) 3D printed PEG-based hybrid nanocomposites obtained by sol-gel technique. *ACS Appl Mater Interfaces* 8(8):5627–5633. [https://doi.org/10.1021/ACSAMI.5B12578/SUPPL\\_FILE/AM5B12578\\_SI\\_001.PDF](https://doi.org/10.1021/ACSAMI.5B12578/SUPPL_FILE/AM5B12578_SI_001.PDF)
39. Fantino E et al (2016) 3D printing of conductive complex structures with in situ generation of silver nanoparticles. *Adv Mater* 28(19):3712–3717. <https://doi.org/10.1002/adma.201505109>
40. Paul DR, Robeson LM (2008) Polymer nanotechnology: nanocomposites. *Polymer (Guildf)* 49(15):3187–3204. <https://doi.org/10.1016/J.POLYMER.2008.04.017>
41. Cortés A, Sánchez-Romate XF, Jiménez-Suárez A, Campo M, Ureña A, Prolongo SG (2020) Mechanical and strain-sensing capabilities of carbon nanotube reinforced composites by digital light processing 3D printing technology. *Polymers* 12(4):975. <https://doi.org/10.3390/POLYM12040975>
42. Ratkowsky DA (1990) *Handbook of nonlinear regression models*. Marcel Dekker, New York
43. Manapat JZ, Mangadiao JD, Tiu BDB, Tritchler GC, Advincula RC (2017) High-strength stereolithographic 3D printed nanocomposites: graphene oxide metastability. *ACS Appl Mater Interfaces* 9(11):10085–10093. <https://doi.org/10.1021/acsami.6b16174>
44. Mahmoudifard M, Safi M (2012) Novel study of carbon nanotubes as UV absorbers for the modification of cotton fabric. *103(8):893–899*. <https://doi.org/10.1080/00405000.2011.622461>
45. Bastani S, Darani MK, Bastani S, Darani MK (2016) Carbon nanotube-based UV-curable nanocomposite coatings. *Carbon Nanotubes Curr Progr Polym Compos*. <https://doi.org/10.5772/62507>
46. Pal G, Kumar S (2016) Multiscale modeling of effective electrical conductivity of short carbon fiber-carbon nanotube-polymer matrix hybrid composites. *Mater Des* 89:129–136. <https://doi.org/10.1016/j.matdes.2015.09.105>
47. Kang I, Schulz MJ, Kim JH, Shanov V, Shi D (2006) A carbon nanotube strain sensor for structural health monitoring. *Smart Mater Struct* 15(3):737–748. <https://doi.org/10.1088/0964-1726/15/3/009>
48. Obitayo W, Liu T (2012) A review: carbon nanotube-based piezoresistive strain sensors. *J Sens* 2012. <https://doi.org/10.1155/2012/652438>
49. Alamusi, Hu N, Fukunaga H, Atobe S, Liu Y, Li J (2011) Piezoresistive strain sensors made from carbon nanotubes based polymer nanocomposites. *Sensors (Basel)* 11(11):10691–10723. <https://doi.org/10.3390/S111110691>
50. Kumar S, Gupta TK, Varadarajan KM (2019) Strong, stretchable and ultrasensitive MWCNT/TPU nanocomposites for piezoresistive strain sensing. *Compos B Eng* 177(March):107285. <https://doi.org/10.1016/j.compositesb.2019.107285>
51. Ubaid J, Schneider J, Deshpande VS, Wardle BL, Kumar S (2022) Multifunctionality of nanoengineered self-sensing lattices enabled by additive manufacturing. *Adv Eng Mater* 24(7):2200194. <https://doi.org/10.1002/ADEM.202200194>

**Publisher's note** Springer Nature remains neutral with regard to jurisdictional claims in published maps and institutional affiliations.